Ocean Dynamics (2014) 64:29–46
DOI 10.1007/s10236-013-0668-3

A statistical description on the wind-coherent responses of sea surface heights off the US West Coast

Sung Yong Kim

Received: 30 October 2012 / Accepted: 30 October 2013 / Published online: 22 November 2013

Abstract Local and remote wind-coherent responses of sea surface heights (SSHs) off the US West Coast (USWC) are described with statistical and analytical models. The wind transfer functions are statistically derived from surface wind stress at National Data Buoy Center (NDBC) buoys, located within 50 km from the shoreline, and detided SSHs (SSH anomalies; SSHAs) at shoreline tide gauges for 15 years (1995 to 2009) using linear regression in the frequency domain. A two-dimensional analytical model constrained by the coastal boundary provides a dynamical framework to interpret the data-derived statistical model. Although both transfer functions agree well at low frequency [$\sigma \leq 0.4$ cycles per day (cpd)], they appear to be inconsistent at high frequency ($\sigma \geq 0.8$ cpd; e.g., diurnal and its harmonic frequencies) because of incoherent signals between wind stress and SSHAs as well as their low signal-to-noise ratios. A multivariate regression analysis using wind stress at multiple wind buoys is implemented with a modified expectation maximization. The cross-validated skill increases and becomes saturated as the number of regression basis functions increases, demonstrating the influence of local and remote winds. The skill computed from all available winds off the USWC has a maximum as 0.1 in southern California, 0.2 to 0.3 in central California, and 0.3 to 0.5 in northern California, Oregon, and Washington. The residual SSHAs, incoherent components with all available coastal wind stress off the USWC, still contain poleward propagating signals, considered as components forced by remote winds outside of the domain.

Keywords Sea surface heights · Coastal winds · Transfer functions

Responsible Editor: Aida Alvera-Azcárate

S. Y. Kim (✉)
Division of Ocean Systems Engineering, School of Mechanical, Aerospace & Systems Engineering, Korea Advanced Institute of Science and Technology, 291 Daehak-ro, Yuseong-gu, Daejeon 305-701, Republic of Korea
e-mail: syongkim@kaist.ac.kr

1 Introduction

The wind-driven circulation in coastal regions is a complicated dynamical response associated with stratification, baroclinic alongshore pressure gradients, Earth rotation, friction, bottom topography, and vertical mixing of heat and momentum transferred by local and remote winds (e.g., Allen 1980; Winnant 1980; McCreary 1981; Brink 1991). The upwelling-favorable winds generate an offshore transport in surface waters, which leads to upwelling of colder subsurface water, i.e., upward sloping of isopycnals toward the coast, and dropping of the sea surface height (SSH)[1] at the coast. As a response to the onshore sloping SSH, the geostrophic currents form in the wind direction. In a similar way, the downwelling-favorable winds yield an onshore transport and depress the thermocline as a result of piled-up warmer water at the coast. Then, the offshore sloping SSH generates geostrophic currents aligned with the wind direction (e.g., Chelton and Enfield 1986; Lentz 1995; Brink 1998). In the wind-forced subsurface circulation near the coast, the isopycnals are tilted in an opposite sense of SSHs, and their geostrophic balance is closely related to the generation of the coastal undercurrents. These coastal

[1] Although atmospherically adjusted, SSH is referred to as adjusted sea level (ASL) or synthetic subsurface pressure (SSP) (e.g., Strub and James 1988; Harms and Winant 1994), they are denoted as the SSH shortly throughout the paper (see Section 2.2 for more details).

undercurrents appear in most eastern ocean boundaries and have a tendency to deepen and weaken toward the pole. The baroclinic (near-surface) alongshore pressure gradient is taken into account as one of the primary driving forces of coastal undercurrents (e.g., Wooster and Jones 1970; Brink et al. 1978; McCreary 1981; Gay and Chereskin 2009).

The current responses to the coastal wind are considered to be anisotropic and asymmetric because the geostrophic balance of local pressure setup against the coast in the cross-shore direction and the frictional balance to wind stress in the alongshore direction are not symmetric (e.g., Gonella 1972; Weller 1981; Kim et al. 2009, 2011). This anisotropic response was initially acknowledged by Ekman (1905) with qualitative descriptions by allowing for the angle between the wind direction and the coastline. Weisberg et al. (2001) reported that stratification can cause an asymmetric response wherein the offshore scale and magnitude of the upwelling responses are larger than those for the downwelling responses (e.g., Allen et al. 1995; Austin and Lentz 2002). Moreover, the wind-forced circulation may be modified under asymmetric and varying bottom topography (e.g., O'Brien et al. 1977; Pringle 2002; Castelao and Barth 2005).

The wind-driven circulation in the alongshore direction is characterized by alongshore pressure gradients and coastally trapped waves (CTWs). Alongshore pressure gradients are typically driven by atmospheric pressure setup including upwelling-favorable winds and their relaxation and reversal (e.g., Kosro 1987; Largier et al. 1993; Winant et al. 2003). On the other hand, shelf topography and stratification in coastal regions play a crucial role in the formation of propagating waves along the coast such as barotropic shelf waves and baroclinic internal waves, respectively. When both waves are present under the Coriolis effect, the waves are trapped near the coast in the form of barotropic continental shelf waves and internal Kelvin waves (e.g., Huthnance 1981; Brink 1991).

Numerous studies have enhanced understanding on the SSH responses to local and remote winds, for example, CTWs, barotropic Kelvin waves, climate signals, and storm surge (e.g., Gill and Schumann 1974; Platzman 1979; Csanady 1980; Davis and Bogden 1989). Those studies have been initiated with the statistical analysis of observed winds and detided SSHs (SSH anomalies; SSHAs) off the US West Coast (USWC) such as the space-lagged cross-correlations and cross-spectra in the time and frequency domains. Wang and Mooers (1977) interpreted poleward propagating SSHAs as forced and free CTWs depending on the degrees of resonance with coastal winds (see Clarke (1977) for other historical observations). Coastal winds to the south of a location lead the SSHAs in time as poleward propagating signals in summer off the USWC (e.g., Enfield and Allen 1983; Halliwell and Allen 1984; Allen and Denbo 1984). As an opposite case, the equatorward propagating signals in winter in this region are regarded as the occasional winter storm events (e.g., Mooers and Smith 1968). Spillane et al. (1987) and Enfield (1987) developed a discussion on locally and remotely forced SSHAs at basin-wide and multi-annual scales. They reported that the poleward SSHAs are activated from the central equatorial Pacific and have a consistent phase speed of the first mode CTWs. Recently, Ryan and Noble (2006) interpreted that CTWs and climate signals (e.g., El Niño-Southern Oscillation (ENSO)) were forced by regional and basin-wide winds, respectively, using wind transfer functions on SSHAs off the USWC. However, the influence of local and remote winds was not clearly described because there was ambiguity in determining the locally and remotely forced SSHs with the regression conducted with a pair of wind stress and SSH time series at a single location. With the help of computational resource, realistic numerical models have substantiated the coastal circulation due to local and remote forces (e.g., Pares-Sierra and O'Brien 1989). Pringle and Dever (2009) examined the influence of alongshore winds, bathymetry, and basin-scale pressure gradients on the coastal upwelling and relaxation. They confirmed that alongshore pressure gradients are closely related to the California Undercurrent (CU) (e.g., McCreary 1981) and that the shelf width is inversely proportional to the strength of both upwelling and alongshore flows (e.g., Pringle 2002).

Although the terms of 'local' and 'remote' forces in the coastal circulation have been used in several ways, they are not clearly defined and understood. As a simple definition, the remote force has been considered as alongshore pressure gradients including nonlocal effects as opposed to the influence of the local wind (e.g., Davis and Bogden 1989; Lopez and Clarke 1989). Similarly, the magnitude of upwelling, which can be correlated with the alongshore flows and alongshore pressure gradients, can be a factor to differentiate the local and remote forcing (e.g., Hickey and Pola 1983; Pringle and Dever 2009). As a regional example of winds, local and remote winds were referred to as coastal winds off California and equatorial trade winds in Pacific, respectively (e.g., Enfield and Allen 1980; Pares-Sierra and O'Brien 1989; Clarke and Lebedev 1999). Thus, the local and remote winds may be taken into account in the context of decorrelation length and time scales of the interested atmospheric and oceanic variability.

In describing and characterizing the system, two primary approaches—statistical and dynamical models—have been examined. The statistical analysis using a transfer function (or Green's function) has been used for data analysis and signal processing in oceanographic and engineering communities (e.g., Emery and Thomson 1997; Oppenheim

et al. 1998). The transfer function represents a unique relationship between forcing and response to identify and characterize the system. On the other hand, the dynamical model using governing equations describes the system with interlocked dynamical components. As individual approaches may have limitations, these two approaches complement each other and enrich our understanding on the given system. For instance, the stochastic processes require enough realizations of both forcing and response in order to have estimates with statistical significance. Not all systems have the governing equations, and the relevant dynamical terms are not always defined explicitly. Thus, in this paper, two approaches are applied to an example that wind stress and sea surface heights are primary players (see Kim et al. (2013a) for the case of wind stress and currents).

A novelty of this study lies in a comprehensive analysis to address the local and remote wind-coherent SSH responses with the help of both statistical and analytical models. The statistical model, i.e., wind transfer function, is derived from historical observations of coastal wind stress and SSHAs off the USWC. A statistical regression—a modified expectation maximization (EM)—allows making the best use of available wind observations regardless of missing data, which is an extended analysis of what Ryan and Noble (2002, 2006) conducted (Section 3.1.2). A two-dimensional analytical model constrained by the coastal boundary provides a dynamical framework to interpret the statistical model (Sections 3.2 and 4.1). While the wind transfer functions derived from a three-dimensional numerical model are discussed elsewhere (e.g., Kim et al. 2013a), the proposed model will provide basic information to explain the local wind-driven SSHs and relevant dynamics.

This paper is organized into four sections. The observations of the wind and SSHs are summarized in Section 2, and the wind transfer functions derived from statistical and analytical models are described in Section 3. In Section 4, the comparison of wind transfer functions, the characterization of local and remote wind-forced SSHAs using the cross-validated skill are discussed. The final comments on wind-driven SSHs are presented in Sections 5 and 6.

2 Summary of observations

2.1 Coastal surface winds

The hourly surface winds[2] at 18 National Data Buoy Center (NDBC) buoys off the USWC, located within 50 km from the shoreline, for 15 years (1995 to 2009) are analyzed (Figs. 1 and 2a; Table 1). As shore-based wind data (e.g., C-Man stations) may contain a bias due to land effects, they were not included. The principal axes of coastal surface winds off the USWC are nearly parallel to the coastline (e.g., Dorman and Winant 1995), and the cross-shore and alongshore wind components are defined as normal and parallel to the principal axes.

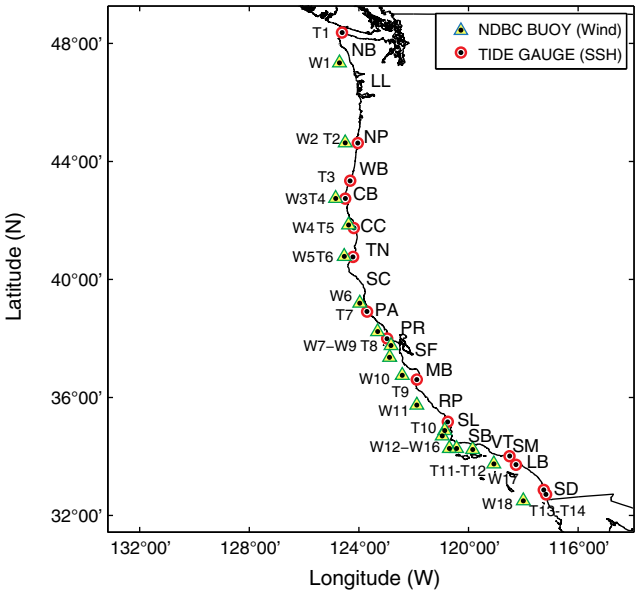

Fig. 1 A study domain for investigation of local and remote wind-coherent sea surface heights. The NDBC wind buoys (Table 1) and shoreline tide gauge stations (Table 2) on the USWC are indicated as *green triangles* and *red circles*, respectively. For reference, the locations of some coastal regions along the USWC are denoted by abbreviated two letter names: San Diego (*SD*), Long Beach (*LB*), Santa Monica (*SM*), San Buenaventura (*VT*), Santa Barbara Channel (*SB*), Port San Luis (*SL*), Ragged Point (*RP*), Monterey Bay (*MB*), San Francisco (*SF*), Point Reyes (*PR*), Point Arena (*PA*), Shelter Cove (*SC*), Trinidad (*TN*), Crescent City (*CC*), Cape Blanco (*CB*), Winchester Bay (*WB*), Newport (*NP*), Loomis Lake (*LL*), and Neah Bay (*NB*)

Variability of coastal surface winds off the USWC is characterized with subinertial alongshore winds and diurnal land/sea breezes (e.g., Dorman and Winant 1995). The subdiurnal winds explain 50 to 80 % of total variance of coastal winds; 50 % in southern California, 65 % in central California, and 80 % in northern California and Oregon (not shown) (e.g., Largier et al. 1993; Dorman and Winant 1995). The spatial scales of the alongshore winds are estimated differently in two regions of northern and southern areas of Point Conception (e.g., Caldwell et al. 1986). The diurnal and its harmonically related winds take 10 to 25 % of total variance, and their variability depends on the distance from the shoreline due to the development of the marine boundary layer (e.g., Estoque 1961; Atkins and Wakimoto 1997).

The long-term mean of cross-shore winds (u) is very weak (less than 0.3 m s^{-1}), compared to the time-mean of alongshore winds (v), which has a maximum in northern and central California of ~7 m s^{-1} and decreases to 1 to 3 m s^{-1}

[2]The winds indicate the wind vector components (u and v) unless explicitly stated otherwise.

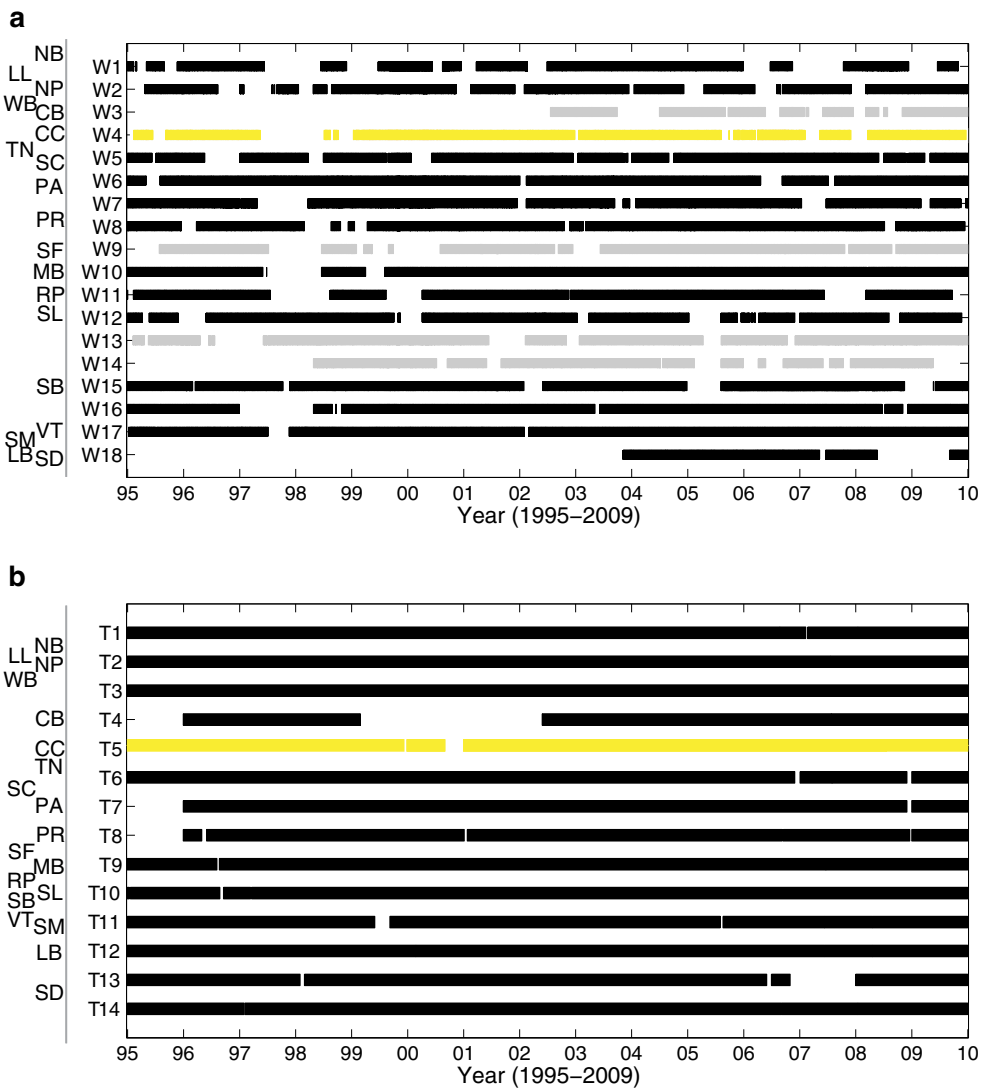

Fig. 2 Data availability of (**a**) coastal winds at NDBC buoys and (**b**) SSHs at tide gauges off the USWC for 15 years (1995 to 2009). A pair of observations of the wind at St. Georges (W4 in Fig. 1) and SSHA at Crescent City (T5 in Fig. 1) is denoted as *bright yellow bars* (see Section 4.1 and Fig. 5). Winds at four stations (*gray bars*) are not considered in the modified EM (see Sections 1 and 4.2)

off Oregon and southern California (Fig. 3a). The standard deviation (STD) of alongshore winds increases with latitude as ∼7.3 m s^{-1} at Port Orford (W3) and decreases to the south by ∼3 m s^{-1} or so except for an anomalous wind speed at Point Conception (∼5.6 m s^{-1}). This may result from the geophysical shading and the regional atmospheric fronts (e.g., Brink et al. 1984; Skyllingstad et al. 2001). The STD distribution of alongshore winds is consistent with other coastal wind observations off the USWC during other time periods (e.g., Chapman 1987; Halliwell and Allen 1984, 1987; Strub et al. 1987; Dorman and Winant 1995; Winant and Dorman 1997) (Fig. 3b). The STD of cross-shore winds is almost uniform over the entire coast with approximately half of the STD of alongshore winds. On the other hand, García-Reyes and Largier (2010) conducted multi-year data analysis of coastal winds off the USWC (1982 to 2009) and reported that the upwelling-favorable winds in central California (35 °N to 39 °N; RP to SC in Fig. 1) have become stronger and led the enhanced and longer upwelling due to changes in the strength of large-scale atmospheric pressure gradient field.

There are several choices of drag coefficients in converting wind observations to wind stress. In the low wind speed regime (less than 5 m s^{-1}), the drag coefficients can increase (e.g., Large et al. 1995; Yelland and Taylor 1996), hold constant (e.g., Large and Pond 1981), or decrease (e.g., Garratt 1977). However, in the moderate regime (between 5 and 15 m s^{-1}), they have similar values or a slightly increasing tendency (e.g., Foreman and Emeis 2010). A typical wind speed on the USWC is more than 5 m s^{-1} except for southern California (Fig. 3b). Thus, the choice of wind drag coefficients is likely to be insensitive to the overall results.

Table 1 NDBC wind buoys off the USWC used in this analysis (Figs. 1 and 2a). The principal axis is defined as the tilt angle of the major axis in a counterclockwise sense from true North (degrees)

Station	Station ID	Station name	Latitude (°N)	Longitude (°W)	Principal axis (°T)
W1	46041	Cape Elizabeth	47.34	124.71	317.1
W2	46050	Stonewall Bank	44.63	124.50	358.5
W3	46015	Port Orford	42.75	124.85	357.2
W4	46027	St. Georges	41.85	124.38	335.3
W5	46022	Eel River	40.78	124.54	351.0
W6	46014	Pt. Arena	39.20	123.97	326.0
W7	46013	Bodega Bay	38.23	123.32	315.1
W8	46026	San Francisco	37.76	122.83	321.3
W9	46012	Half Moon Bay	37.36	122.88	327.3
W10	46042	Montrey Bay	36.75	122.42	323.2
W11	46028	San Martin	35.74	121.89	319.8
W12	46011	Santa Maria	34.88	120.87	321.1
W13	46023	Pt. Arguello	34.70	120.96	320.9
W14	46063	Pt. Conception	34.27	120.70	322.4
W15	46054	W. Santa Barbara	34.27	120.44	306.5
W16	46053	E. Santa Barbara	34.24	119.85	277.1
W17	46025	Santa Monica	33.75	119.08	288.0
W18	46086	San Clemente Basin	32.50	118.00	303.0

Drag coefficients from Yelland and Taylor (1996) are used for following analysis to get wind stress.

The directional steadiness (γ) of the wind is defined as the ratio of the magnitude of the time-averaged wind components to the time-mean of wind speed (Chelton et al. 2007; Singer 1967):

$$\gamma = \frac{\sqrt{\langle u \rangle^2 + \langle v \rangle^2}}{\langle \sqrt{u^2 + v^2} \rangle}. \quad (1)$$

For constant directional winds, the steadiness is equal to 1 regardless of the change of wind speed. When the wind direction varies, the steadiness decreases and approaches 0. The steadiness of coastal winds off the USWC varies from 0.5 to 0.7 in the California coast and from 0.2 to 0.1 in the Oregon and Washington coast (Fig. 3c). As the steadiness has seasonality, the estimate from the entire year record may reflect the dominant character of the wind direction. Thus,

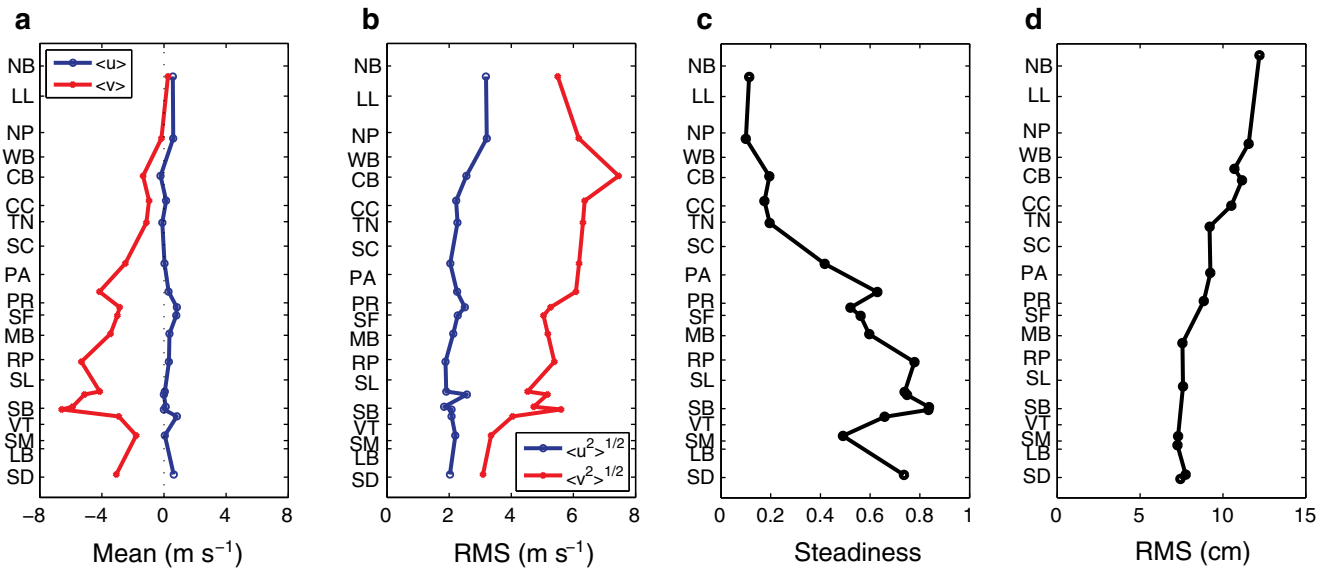

Fig. 3 **a** Mean, **b** standard deviation (STD), and **c** steadiness of the coastal winds in the cross-shore (u) and alongshore (v) directions. The wind components are rotated into the principal axes (Table 1). **d** Standard deviation of the detided SSHs (SSHAs). See Fig. 1 for the abbreviated name of coastal regions

Fig. 3c showed a tendency differing from the steady wind setup during summer off USWC (Chelton et al. 2007).

As the atmospheric forcing generated in the south of Baja California (23 °N) can be dissipated in the Gulf of California (e.g., Enfield and Allen 1983; Spillane et al. 1987; Ramp et al. 1997), the effective atmospheric remote forcing to derive the SSHA variability off the USWC may be initiated near the north of Baja California.

2.2 Sea surface heights

Hourly SSHs at 14 shoreline tide gauges on the USWC for the same time period of the NDBC winds are used (Figs. 1 and 2b; Table 2). The measured SSHs (η) relative to the North American Vertical Datum (NAVD) are adjusted with the atmospheric pressure provided by the NCEP/NCAR reanalysis data (Kalnay et al. 1996) in order to remove the inverted barometer effect (e.g., Agnew 1986; Wunsch and Stammer 1997). The tide gauge stations used in this analysis are selected when they have an effective spatial coverage over the entire USWC and temporal coverage over the chosen time window as well as statistical consistency between stations (e.g., correlation and coherence). For instance, the tide gauge stations inside San Francisco Bay (e.g., San Francisco, Redwood City, Alameda, Richmond, and Mare Island (CA)), Willapa Bay (e.g., Toke Point (WA)), and Columbia River (e.g., Hammond and Astoria (OR)) were excluded because of potential bay effects and anomalously reduced correlation with other stations. Furthermore, Oil Platform Harvest (CA), Garibaldi (OR), and Westport (WA) stations are not included due to the relatively short record length (e.g., shorter than 11 years).

The STD of the detided SSHs (η_F) has a tendency to increase from south to north from 7 to 12 cm (Fig. 3d) (see Section 3.1.1 for more details). This nontidal variance reflects partially the wind-driven SSHAs in the subinertial frequency band (e.g., Davis and Bogden 1989).

As SSHs at tide gauges may contain instrumental errors and the tide gauges are not located closely together, the SSH gradients in the alongshore and cross-shore directions ($\partial\eta/\partial x$ and $\partial\eta/\partial y$) may not be significant and useful for further analysis (e.g., Agnew 1986; Lentz 1993; Harms and Winant 1994). Thus, this study focuses on the relationship between wind stress and SSHs instead of SSH gradients.

3 Statistical and analytical models

In this section, details of two models derived from statistical and dynamics frameworks are described. First, in order to derive transfer functions using multivariate regression in the frequency domain, an overview on the decomposition of SSH data (Section 3.1) and the required systematic preprocessing of the data (e.g., removal of inverted barometer effect, surface tides, and long-term mean) (Section 3.1.1), and the statistical formulation for derivation of the transfer function (Section 3.1.2) will be discussed. Then, the two-dimensional analytic model is presented for dynamical interpretation of transfer functions (Section 3.2) (Fig. 4).

3.1 Statistical model

The SSHs (η) are decomposed into inverted barometer effect (η_B), tide-coherent (η_T), wind-coherent (WSSHs, η_W), and residual components (RSSHs, η_R) as a function of frequency (e.g., Kim et al. 2010a, b):

$$\eta(\sigma) = \eta_B(\sigma) + \eta_T(\sigma) + \eta_F(\sigma). \quad (2)$$

Table 2 NOAA tide gauge stations off the USWC used in this analysis (Figs. 1 and 2b)

Station	Station ID	Station name	Latitude (°N)	Longitude (°W)
T1	9443090	Neah Bay	47.368	124.616
T2	9435380	South Beach	44.625	124.043
T3	9432780	Charleston	43.345	124.321
T4	9431647	Port Orford	42.740	124.496
T5	9419750	Crescent City	41.745	124.183
T6	9418767	North Spit	40.766	124.216
T7	9416841	Arena Cove	38.913	123.708
T8	9415020	Point Reyes	37.996	122.975
T9	9413450	Monterey	36.605	121.888
T10	9412110	Port San Luis	35.176	120.760
T11	9410840	Santa Monica	34.008	118.500
T12	9410660	Los Angeles	33.720	118.271
T13	9410230	La Jolla	32.866	117.258
T14	9410170	San Diego	32.713	117.173

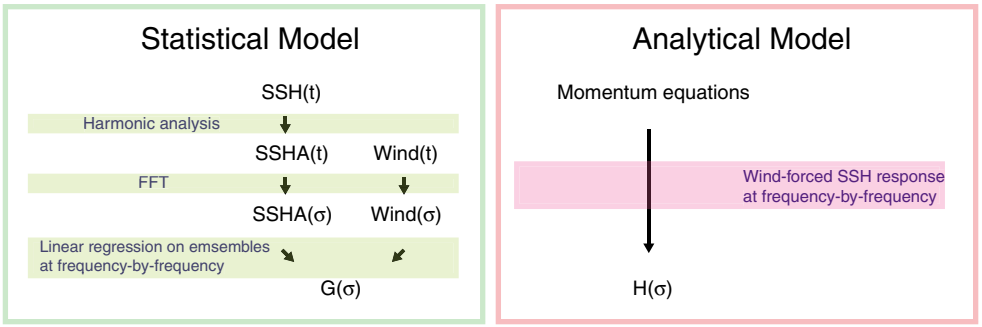

Fig. 4 A procedure to derive statistical and analytical models. The SSH anomaly (SSHA) is the residual of harmonic analysis on the SSH. The Fourier coefficients of both SSHA and wind time series are used to compute the transfer function [G(σ)] by linear regression of their ensembles at frequency-by-frequency. On the other hand, the transfer function [H(σ)] in the analytic model is derived from terms of wind and SSH in the momentum equations at frequency-by-frequency

where

$$\eta_{\mathrm{F}}(\sigma) = \eta_{\mathrm{LW}}(\sigma) + \eta_{\mathrm{LWR}}(\sigma), \quad (3)$$

$$= \eta_{\mathrm{RW}}(\sigma) + \eta_{\mathrm{RWR}}(\sigma), \quad (4)$$

and WSSHs can be considered as local or remote WSSHs (η_{LW} and η_{RW}) and corresponding RSSHs (η_{LWR} and η_{RWR}). The difference between local and remote WSSHs ($\eta_{\Delta\mathrm{RL}}$) is attributed to only remote winds because spectral contents at low frequency in the local WSSHs can be isolated:

$$\eta_{\Delta\mathrm{RL}}(\sigma) = \eta_{\mathrm{RW}}(\sigma) - \eta_{\mathrm{LW}}(\sigma). \quad (5)$$

The WSSHs (η_{W}) are computed using wind regression (see Section 3.1.2 for more details) (e.g., Kim et al. 2009, 2010a, b). The residual SSHs (η_{R}) can be the sum of the barometric pressure-coherent SSHs (e.g., storm surge, Heaps 1969, 1983; Flather 1994), nonlinear interactions between barotropic tides (η_{T}), and other forcing responses. However, the SSHs driven by other forces such as the radiation stress and the frictional bottom stress are not included explicitly in this analysis (e.g., Mastenbroek et al. 1993; Nicolle et al. 2009). Although wind stress and SSHs are not dynamically related, they can be coherent at specific frequencies. Thus, variance at those frequencies is removed prior to wind regression. For example, the K_1 tidal frequency is equal to the sum of the seasonal frequency and the diurnal frequency, i.e., 1 cycle per day (cpd)+1/365.2425 cpd = 1.0027 cpd. Therefore, variance of wind stress and SSHs at 1.0027 cpd can appear as coherent signals. Using a least-squares fit (e.g., Pawlowicz et al. 2002; Kim et al. 2010a), variance of wind stress at the seasonal frequency (SA_1) and its six harmonic frequencies ($SA_2 \cdots SA_6$) and that of SSHs at all available tidal frequencies (approximately 150 frequencies in Pawlowicz et al. (2002) including M_2, K_1, O_1, P_1, S_2, SA_1, $SA_2 \cdots SA_6$) are filtered out. While wind stress and SSHs contain seasonal variance up to four harmonic frequencies, the energy at six seasonal harmonic frequencies is excluded as a conservative way. Moreover, variance of spring–neap (SP, difference of M_2 and S_2 frequencies) and lunar fortnightly (MF, difference of K_1 and O_1 frequencies) tides is also filtered out because they are not related to winds. As the seasonality and its harmonic variance in SSHs are removed, the influence of seasonal heat flux on SSHs is not included.

3.1.1 Data filtering and significance

The long-term time mean in both data sets of observed wind stress and SSHAs is removed, respectively, and no band-pass filters are applied. The number of degrees of freedom (DOF, $2N$) in the spectral analysis is determined by a trade-off between the frequency resolution and confidence level of estimates. In other words, as the DOF increases, the frequency resolution of the estimates gets wider while the error bars become smaller. A single time series is broken into N nonoverlapped time series with identical record lengths, then the spectral analyses for the individual segments are averaged (e.g., Bendat and Piersol 2000; Kim et al. 2010a). In this paper, the power spectra and transfer functions are ensemble-averaged over 200 Fourier coefficients computed from nonoverlapped 27-day-long time series, which allows the reasonable confidence interval estimate. As the number of ensembles increases, the structure of power spectra and transfer functions in the frequency domain (e.g., peaks and noisy fluctuations) becomes evident. However, the overall estimates are less sensitive to the choice of the DOF. When the number of missing observations is more than 50 % of the length of each chunk, the segmented time series is not included in the estimate (Fig. 2). Thus, the fractional data availability to participate in the following estimates is over 82 %.

In order to handle missing data in both winds and SSHAs time series, the slow finite Fourier transform (FFT) and regular FFT can be applicable. In the slow FFT, the Fourier coefficients are estimated for this entire frequencies, a

finite frequency axis corresponding to the regular FFT (see Appendix B), by solving an inverse problem. Although the slow FFT is computationally expensive, the missing data in the time series can be taken care of appropriately. On the other hand, an ad hoc approach to fill the missing data of demeaned time series with zeros prior to the regular FFT can be also applicable. Comparison of Fourier coefficients of the slow FFT-ed and regular FFT-ed time series with missing data shows minor difference at high frequency ($\sigma > 3$ cpd), depending on the fraction of missing data.

As performance of the regression depends on the quality of regression basis functions (e.g., wind data in this paper), the missing data in wind time series are gridded with the sample data covariance matrix (e.g., Kim et al. 2007; Wunsch 1996). The sample data covariance is obtained from hourly wind observations at 15 NDBC buoys for 15 years (1995 to 2009). However, the difference in the estimates using gridded and raw wind data is negligible because the proposed EM and regularization can reduce noise and potential artifacts associated with treatment of missing data. No window functions are applied to individual segments in order to keep variance at low frequency. The model- and data-derived transfer functions are nearly consistent at low frequency (Fig. 5c and e), which can justify to include low-frequency variance in the individual segments in the following analysis.

Error bars of power spectra, coherence, and transfer functions (Figs. 5 and 8) are computed from either the 95 % confidence interval or the Jackknife method (e.g., Priestley 1981; von Storch and Zwiers 1999; Bendat and Piersol 2000). On the other hand, Monte Carlo simulations can be performed to estimate the statistical significance of the coherence and phase (e.g., Ebisuzaki 1997). A model time series is generated to have the same variance as observations, and its phase is randomized by applying a sequence of Fourier transform, i.e., a product of a unit random complex number and Fourier coefficients of the time series, then its inverse Fourier transform. Then, the coherence and phase between model data and observations become the uncertainty of estimates.

3.1.2 Wind regression

Wind regression is a least-squares fit using the wind stress for the basis functions of regression (e.g., Kim et al. 2009, 2010a, b). The regression coefficients are regarded as the transfer function in the frequency domain or the response function in the time domain. The wind transfer function ($\mathbf{G}$) of SSHs is computed from covariance matrices of Fourier coefficients of SSHAs (η_{F}) and wind stress ($\boldsymbol{\tau}$):

$$\mathbf{G}(\sigma) = \left(\langle \eta_{\mathrm{F}}(\sigma)\, \boldsymbol{\tau}^{\dagger}(\sigma)\rangle\right)\left(\langle \boldsymbol{\tau}(\sigma)\, \boldsymbol{\tau}^{\dagger}(\sigma)\rangle + \mathbf{R_a}\right)^{-1}, \qquad (6)$$

where $\mathbf{R_a}$ denotes the regularization matrix to control the error and noise embedded in the impulse (wind stress) and to adjust variance of the regressed data (WSSHs) (e.g., Inman 1975; Tikhonov and Arsenin 1977; Constable et al. 1987; Wunsch 1996) († indicates complex conjugate transpose or matrix transpose). While $\mathbf{R_a}$ can be a function of frequency, it is assumed to be a diagonal matrix scaled by a constant value for simplicity over all frequencies because noise at different frequencies may not be coherent to each other. The missing data in the time series of wind stress may turn into its covariance matrix to be nonpositive definite matrix, i.e., noninvertible matrix. Thus, $\mathbf{R_a}$ can make the covariance matrix positive definite. Moreover, as the trace of $\mathbf{R_a}$ increases, variance mapped by the transfer function ($\mathbf{G}$) decreases, which leads to lower variance of WSSHs (η_{W}). In other words, $\mathbf{R_a}$ keeps the regression from overfitting and underfitting (e.g., Davis 1985; Kim et al. 2009, 2010b). The constant regularization may cause sensitive estimates at high frequency when the noise level is higher than that of regularization. Similarly, this regularization can be applied to the estimate of the response function in the time domain (e.g., Chelton et al. 1988; Kim et al. 2009).

The phase of the transfer function is

$$\boldsymbol{\Theta}(\sigma) = \tan^{-1}\frac{\mathrm{Im}[\mathbf{G}(\sigma)]}{\mathrm{Re}[\mathbf{G}(\sigma)]}. \qquad (7)$$

The WSSHs in the frequency domain are given by the product of the data-derived transfer function and the Fourier coefficients of wind stress,

$$\eta_{\mathrm{W}}(\sigma) = \mathbf{G}(\sigma)\boldsymbol{\tau}(\sigma). \qquad (8)$$

The cross-validated skill on the SSHs, i.e., the fraction of variance explained by wind stress, is defined as

$$\kappa^2(\mathbf{x}) = 1 - \frac{\sum_n |\eta_{\mathrm{R}}(\mathbf{x}, \sigma_n)|^2}{\sum_n |\eta_{\mathrm{F}}(\mathbf{x}, \sigma_n)|^2}, \qquad (9)$$

where n is the indices in the frequency axis and can be used in the computation of the skill in the specific frequency band. $\mathbf{x}$ denotes the location of tide gauge stations in the alongshore direction. The transfer function estimated from training data is applied to independent testing data, and the skill from the testing data will be the cross-validated skill (e,g., Efron and Gong 1983; LeBlanc and Tibshirani 1996). The total data were divided into 90 % training data and 10 % testing data in this paper.

In a similar way, the WSSHs at a single tide gauge can be presented with transfer functions ($\mathbf{G}_l$) and wind stress ($\boldsymbol{\tau}_l$) at multiple wind buoys (e.g., Kim et al. 2010b):

$$\eta_{\mathrm{W}}(\sigma) = \sum_{l=1}^{L} \mathbf{G}_l(\sigma)\boldsymbol{\tau}_l(\sigma), \qquad (10)$$

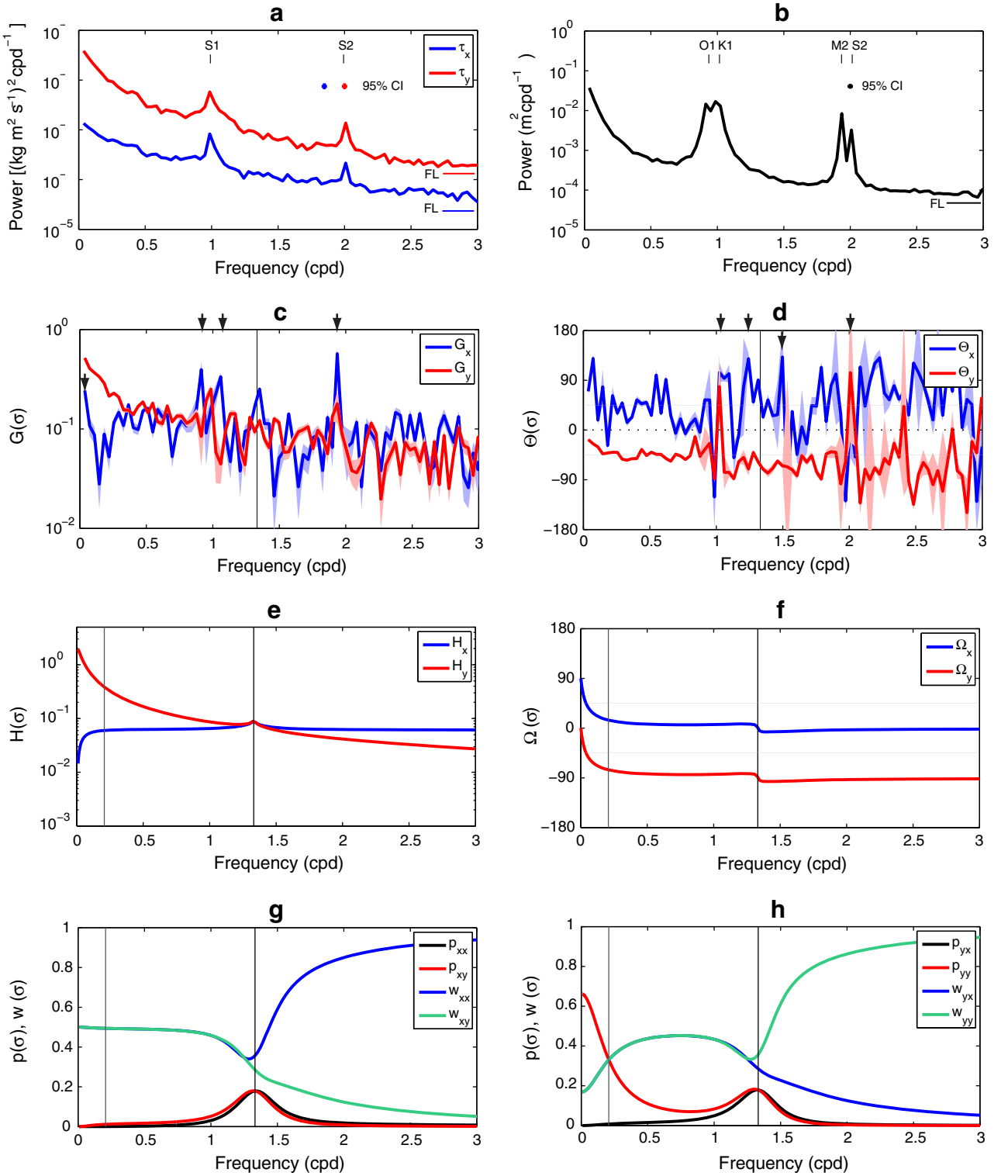

Fig. 5 **a** and **b**: Power spectra of the wind stress at St. Georges (W4 in Fig. 1) and the SSHA at Crescent City (T5 in Fig. 1) for 15 years (1995 to 2009). The W4 buoy is located 8NM northwest of the T5 station. The 95% confidence interval (CI) of individual spectra and the floor level (FL) of variance are indicated. **c** and **d**: Wind transfer functions estimated from observations in **a** and **b**. *Black arrows* indicate the frequency bins where the data-derived transfer function have anomalous estimates compared with the model-derived transfer function. **e** and **f**: Wind transfer functions at surface derived from an analytic model at a depth h ($h = 2\delta_E, \delta_E$ is the Ekman depth). **c** and **e** are magnitudes and **d** and **f** are phases of the transfer functions, respectively. **g** and **h**: Variance contribution on the u component and v component of surface currents (Eqs. 19 and 20). The *vertical gray* and *black lines* indicate the transition frequency (σ_s) and the local inertial frequency ($f_c = 1.332$ cpd), respectively. w_{xx} and w_{xy} in the subinertial frequency band are overlapped

where L denotes the number of basis functions. The prior information in the multivariate regression can be applicable as a function of distance between sampling locations of the driving force (wind stress) and the response (SSHAs) (e.g., Enfield and Allen 1983). When the basis functions are correlated in either space or time, or both, their attribution can be ambiguous (e.g., Kim et al. 2010b). Thus, the regression basis functions need to be orthogonalized in order to differentiate the contributing variance of each regression bases prior to regression (e.g., successive orthogonalization; see Lanczos (1956) for more details). However, as the proposed multivariate regression only fits the total energy of SSHAs, which is coherent with basis functions, the overlapped variance between basis functions is counted only once in estimates of skill and transfer functions.

3.2 Analytical model

A two-dimensional idealized analytical model in the frequency domain (e.g., Winant 2004, 2007; Ponte 2009) is designed to explain the local wind-driven circulation. The individual terms in the momentum equations are Fourier transformed into the frequency domain (σ), and they are combined into the fourth-order nonhomogeneous ordinary differential equations. The homogeneous solution can be found by characteristic equations. The analytic model is driven by an idealized wind forcing, spatially uniform and periodic wind stress.

The idealized model is set up with a straight coast with relatively small sea level slope in the alongshore (y) direction compared to the slope in the cross-shore (x) direction, and the depth-integrated cross-shore flux is closed:

$$\frac{\partial \eta}{\partial y} \ll \frac{\partial \eta}{\partial x}, \tag{11}$$

$$\int u \, \mathrm{d}z = 0, \tag{12}$$

The bottom bathymetry (h) is assumed to be only a function of the cross-shore distance (x):

$$h = h(x). \tag{13}$$

Two cases of bottom topography are tested with constant depth and linearly increasing depth. The model-derived transfer functions are insensitive on the shape of topography as long as they are outside of the inner shelf where surface and bottom boundary layers merge (e.g., Dever 1997; Lentz et al. 1999). While the detailed dynamical interpretation may warrant a more sophisticated model, this model is sufficient to assess the local wind-driven circulation and SSHs.

In addition, a constant eddy viscosity (ν, $\nu = 5 \times 10^{-4}$ $\mathrm{m^2\ s^{-1}}$) throughout the water column and a no-slip boundary condition at the bottom are applied. The sea level is approximated with a cosine function (see Winant (2007); Ponte (2009) for more details), and the Fourier coefficients of currents ($\hat{u}$ and $\hat{v}$) at a given cross-shore location and depth are solved along with the vertically integrated continuity equation and boundary conditions including no-normal flow condition.

The wind-driven frictional currents ($W_{\{\cdot\}\{\cdot\}}$) can be described with the currents which are parallel and normal to the wind direction. These two primary wind-driven currents may generate the geostrophic currents ($P_{\{\cdot\}\{\cdot\}}$) due to local pressure gradients ($\partial\eta/\partial x$ and $\partial\eta/\partial y$) near the coastal boundaries (e.g., Kim et al. 2013a). As we compute the current response to τ_x and τ_y separately, their decomposed terms at the surface ($z = 0$) are expressed as (e.g., Ponte 2010)

$$\hat{u}(\sigma) = P_{xx}\hat{\tau}_x + P_{xy}\hat{\tau}_y + W_{xx}\hat{\tau}_x + W_{xy}\hat{\tau}_y, \tag{14}$$

$$\hat{v}(\sigma) = P_{yx}\hat{\tau}_x + P_{yy}\hat{\tau}_y + W_{yx}\hat{\tau}_x + W_{yy}\hat{\tau}_y, \tag{15}$$

where the first and second subscripts of currents ($P_{\{\cdot\}\{\cdot\}}$, $W_{\{\cdot\}\{\cdot\}}$) denote the direction of the current and forcing (wind stress), respectively. For example, P_{yx} denotes Fourier coefficients of the v component driven by $\partial\eta/\partial x$ that is related to frictional currents (W_{xx}), generated by τ_x.

In this model, there are opposite and identical pairs of terms related to circulation in the outer shelf:

$$P_{xy}(\sigma) = -P_{yx}(\sigma), \tag{16}$$

$$W_{xy}(\sigma) = -W_{yx}(\sigma), \tag{17}$$

$$W_{xx}(\sigma) = W_{yy}(\sigma). \tag{18}$$

The variance contribution of individual terms is presented as a function of frequency (Fig. 5g and h):

$$p_{ij}(\sigma) = 1 - \frac{T_i^2(\sigma) - P_{ij}^2(\sigma)}{T_i^2(\sigma)}, \tag{19}$$

$$w_{ij}(\sigma) = 1 - \frac{T_i^2(\sigma) - W_{ij}^2(\sigma)}{T_i^2(\sigma)}, \tag{20}$$

where i and j are interchangeable with either x or y,

$$T_x^2 = P_{xx}^2 + P_{xy}^2 + W_{xx}^2 + W_{xy}^2, \tag{21}$$

$$T_y^2 = P_{yx}^2 + P_{yy}^2 + W_{yx}^2 + W_{yy}^2. \tag{22}$$

In this model, the wind-driven SSHs can be inferred from wind-driven pressure gradients (Eqs. 14 and 15). Both transfer functions have very similar shape in the amplitude and phase even though the first order integration in the x direction is required (not shown).

The model-derived transfer functions will be presented $\mathbf{H}$ and $\mathbf{\Omega}$ corresponding to the data-derived transfer functions $\mathbf{G}$ and $\mathbf{\Theta}$ (Eqs. 6 and 7). Their subscripts ($G_{\{\cdot\}}$, $\Omega_{\{\cdot\}}$, $H_{\{\cdot\}}$, or $\Theta_{\{\cdot\}}$) indicate the direction of wind stress. Those symbols are used for the succinct and detailed descriptions of transfer functions.

4 Results

The discussion on data-derived transfer functions is focused on the subdiurnal frequency band ($\sigma \leq 0.8$ cpd) where both wind stress and SSHA have higher SNR than other frequencies. In this paper, the noise level can be assumed as the floor level of energy spectra. Thus, the SNR is the ratio of variance above the floor level to noise (e.g., Kim et al. 2010a; Fig. 3a and b).

4.1 Wind transfer functions

To compute an example of the data-derived wind transfer function, a pair of observations that are located closely together with relatively high wind skill are chosen—wind stress at St. Georges (W4) and SSHAs at Crescent City (T5). Their data availability is shown as green bars in Fig. 2. The W4 buoy is located 8NM northwest of the T5 station, and the wind skill is approximately 0.3. About 30 % of variance can be explained with the local wind, and the rest of variance can be explained with other forces. Note that other candidate pairs of the wind and SSHAs have the skill lower than 0.3. Both wind stress components (τ_x and τ_y) at the W4 buoy have red spectra with small peaks at the diurnal and its harmonic frequencies as a part of atmospheric tides (Fig. 5a) (e.g., Cartwright 1968). The winds in the alongshore and cross-shore directions can have different noise levels, respectively, as 10^{-4} and 5×10^{-5} $(\text{kg m}^2\ \text{s}^{-1})^2\text{cpd}^{-1}$ (Fig. 5a). However, when the noise level of wind observations is assumed to be constant regardless of wind direction (e.g., 5×10^{-5} in Fig. 5a), the SNR of the alongshore wind component is approximately three to five times higher than that of cross-shore one. Similarly, the SSHAs have a red spectrum superposed with enhanced variance (e.g., cusps) centered at diurnal and semidiurnal frequencies (Fig. 5b).

The data-derived wind transfer functions are compared with transfer functions at the surface ($z = 0$) computed from the analytical model in the depth of $2\delta_E$ ($\delta_E = \pi\sqrt{2\nu/f_c}$, δ_E is the Ekman depth)[3] (Fig. 5c to f). In Fig. 5c, G_y appears as a red spectrum with a peak at low frequency. G_x has a low hump at low frequency and fluctuations with a similar order of magnitude compared to G_y. Both H_x and H_y, in general, agree with the shape of both G_x and G_y except for the difference of the shape of G_x and H_x at low frequency ($\sigma \leq 0.2$ cpd) (Fig. 5c and e). At very low frequency ($\sigma \approx 0$ cpd), Θ_y and Θ_x are almost 0° and 90°, respectively, and they transit into −45° and 45° and remain nearly constant with fluctuations at high frequency (Fig. 5d). Θ_y is likely to be well-determined compared to Θ_x due to the difference in SNR. On the other hand, Ω_x and Ω_y are very similar each other with a phase difference of 90 ° (Fig. 5f). Ω_y changes from 0° to −90° and Ω_x does from 90° to 0°, respectively, at the transition frequency ($\sigma_s = 0.22$ cpd, further explanations are given below) and remain near constant above that frequency. Although $\boldsymbol{\Theta}$ and $\boldsymbol{\Omega}$ have nearly consistent signs, they are in a different range (please see below).

The difference between data-derived and model-derived transfer functions can be attributed to stratification, non-negligible alongshore variation of both bottom topography $[O(\partial h/\partial y) \approx O(\partial h/\partial x)]$ and pressure gradients ($\partial\eta/\partial y \gg 1$), bottom friction, an irregular coast, and mismatch of the alongshore wind stress and coastline.

The phase between wind and SSHs depends on bottom friction varying from −90° (no friction) to 0° (friction-dominant) (e.g., Gill and Niiler 1973; Brink et al. 1978), alongshore pressure gradients ($\partial\eta/\partial y$) which was not included in the model, and the alignment between the angle of coastline and wind stress. Moreover, if the alongshore wind stress and the coastline are not aligned ($\theta = 0°$), the balance and transports due to wind-driven pressure gradients and wind stress should be rearranged. Changes as a result of the tilted coastline appear significant at subinertial frequency ($\sigma \leq f_c$) and negligible in other frequencies. As θ increases, the contribution of p_{yx} becomes significant, conversely, the relative fraction of the rest of terms (p_{yy}, w_{yx}, and w_{yy}) is reduced. In turn, H_x increases as much as H_y decreases. In a similar way, as θ increases ($0° \leq \theta \leq 45°$), Ω_x decreases and Ω_y increases. Ω_x and Ω_y vary in a range of −90° to 0° and become identical when θ is equal to 45° (not shown).

Spurious peaks and inconsistent phases in the data-derived transfer functions appear at high frequency (e.g., nearby 0.1, 0.9, 1.1, 1.5, and 1.9 cpd) (black arrows in Fig. 5c and d). The applied constant regularization was used as a cutoff noise level of wind stress. Variance of both wind stress components (τ_x and τ_y) is significantly different as a function of frequency, so the transfer function at high frequency can become sensitive.

This one-dimensional dynamical interpretation is intuitive and convenient. More extensive analysis using a numerical model to present a two-dimensional spatial structure of the wind transfer function on SSHs can be found elsewhere (e.g., Kim et al. 2013a).

The transfer functions derived from idealized analytic model provide connections between dynamical balance and statistical explanation (Fig. 5g and h). In the two-dimensional upwelling theory, the wind-driven transports

[3]The Ekman depth (δ_E) in this paper follows the original definition in Ekman (1905) (e.g., Pond and Pickard 1983), i.e., the depth where subsurface wind-driven currents appear in the opposite direction of the surface currents ($z = \delta_E = \pi\sqrt{2\nu/f_c}$). However, the Ekman depth in most of literature is defined as $\delta'_E = \sqrt{2\nu/f_c}$ (e.g., Madsen 1977; Winant 2006) because it is defined when z/δ'_E is equal to π, i.e., $\delta_E/\delta'_E = \pi$. Thus it does not include the factor of π. The use of the factor of π requires discretion of readers.

normal to the wind direction yield surface pressure gradients against the boundaries where water is piled up, causing geostrophic currents in the direction of wind stress. This geostrophic balance becomes dominant below a transition frequency ($\sigma < \sigma_s$), which is smaller than the spin-up frequency (p_{yy} in Fig. 5h) (e.g., Janowitz and Pietrafesa 1980; Dever 1997). Between σ_s and f_c, the wind-driven frictional currents (W_{yx} and W_{yy} in Fig. 5h) become leading terms in the alongshore currents (Fig. 5h). This transition is closely related to the changes in Ω_x and Ω_y (Fig. 5d and f). On the other hand, the surface pressure gradients driven by wind stress normal to the coastline have relatively weak contribution (p_{xy} in Fig. 5g and p_{xx} in Fig. 5h). Above the inertial frequency ($\sigma \geq f_c$), the currents aligned with the wind direction become dominant (W_{xx} in Fig. 5g and W_{yy} in Fig. 5h).

4.2 Local and remote wind-coherent SSHs

In a view of statistical analysis conducted with coastal observations, two definitions for local and remote winds can be suggested: (1) the wind at a single location and the rest of winds within the domain and (2) all winds within the domain and potential wind forcing outside of the domain (Figs. 7 and 9).

In the regression analysis, the cross-validated skill (Eq. 9) is used as an indicator of the influence of local and remote winds. Considering the SNR of coastal surface wind stress and SSHAs (Fig. 5a and b), cross-validated skills at low frequency ($\sigma \leq 0.4$ cpd) are examined.

The skill for all possible pairs of a single time series of wind stress and the SSHA off the USWC is presented in Fig. 6. Individual estimates are shown as color-coded square, and their optimally interpolated field is presented as the background color. Thus, there is a minor change in colors between squares and the background. The skill increases from 0.05 to 0.15 in southern and central California and from 0.15 to 0.4 in northern California, Oregon, and Washington, consistent with previous works (e.g., Largier et al. 1993). The skill has a maximum in the northern area relative to where the wind station is located. This spatial pattern is invariable for other frequency bands (e.g., $\sigma \leq 1$ cpd and $\sigma \leq 3$ cpd) because primary portion of the skill comes from the subinertial frequency band where the poleward signals are dominant (e.g., Halliwell and Allen 1984; Allen and Denbo 1984; Davis and Bogden 1989).

In a similar way, the locally and remotely forced wind responses are examined with incremental wind regressions using multiple wind basis functions. As the regression basis is added with a constant regularization ($\mathbf{R_a}$ in Eq. 6), the cross-validated skill increases and becomes saturated because all possible variance explained by given basis functions is fitted under applied regularization. This regularization matrix keeps the regression from overfitting and underfitting (e.g., Davis 1985; Kim et al. 2009). As the proposed regression is a least-squares fit of Fourier coefficients at the individual frequencies, the spectral contents overlapped in the multiple basis functions are counted only once. The skill of the SSHA at Crescent city (T5) is computed with most NDBC winds on the USWC. The coastal winds at only 14 stations of 18 stations are used in order to

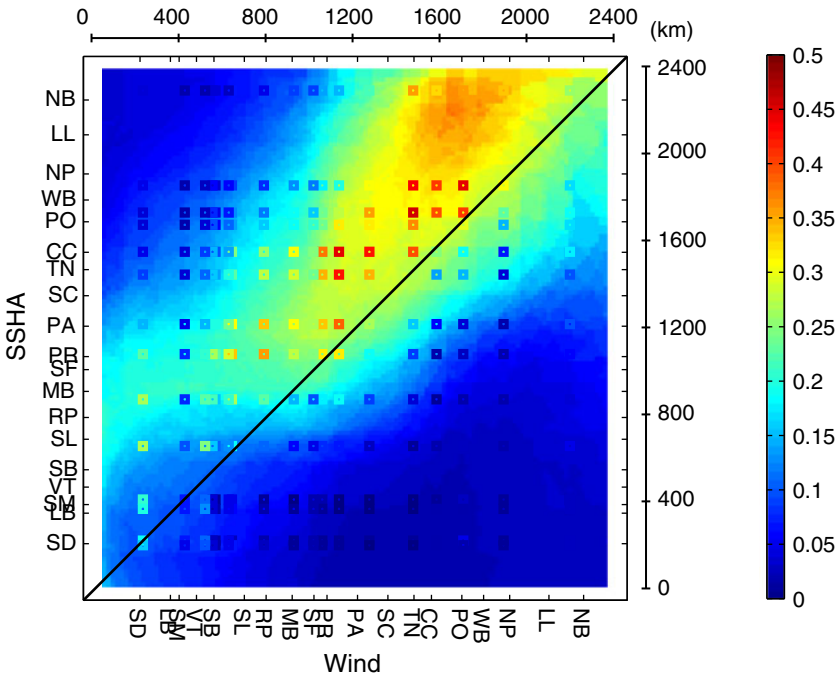

Fig. 6 Cross-validated wind skill (regression using a single wind basis function) with respect to SSHAs off the USWC at low frequency ($\sigma \leq 0.4$ cpd). The relative distance on the USWC is presented with an appropriate scale. The black diagonal line indicates the equidistance region along the coast that the winds and SSHs are sampled at the same location. The physical distance along the coast is shown on the top and right axes

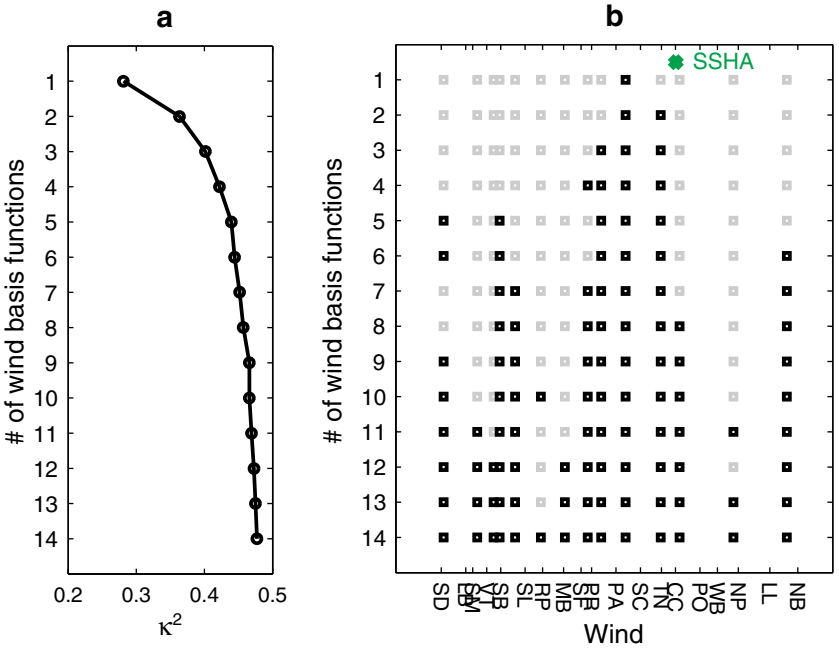

Fig. 7 **a** Cross-validated wind skill (regression using multiple wind basis functions) with respect to SSHAs at Crescent City (T5; The physical location of T5 is marked as a *green cross* on the *top*) at low frequency ($\sigma \leq 0.4$ cpd). **b** Regression basis functions (*black squares*) having maximum wind skill in the regression using a given number of wind basis functions

minimize the spatial bias, which has the wind basis functions equally distributed in space (Fig. 2a). While W13 has a good temporal coverage, it contains more anomalous observations than W12 which needs to increase the regularization in the estimate using modified EM. Moreover, W12 is physically located close to T10. Thus, W13 was not included in the multivariate regression. Figure 7b illustrates the wind stations with a maximum skill (Fig. 7a) in a given number of basis. The contribution of the first four wind bases, located nearby T5 station, is dominant. However, the fractional variance explained by individual winds can be ambiguous. A successive orthogonalization, the removal of coherent components in other bases with respect to a reference basis (e.g., Lanczos 1956; van den Dool et al. 2000), might eliminate this ambiguity. However, this is beyond the scope of this paper.

As an example of local and remote WSSHs (Fig. 8a), η_{LW} and η_{RW} at T5 are computed with wind stress at only single buoy (W4) and 14 buoys (W1, W2, W4 to W8, W10 to W12, and W15 to W18), respectively, which correspond to the skill of 0.28 and 0.48 (Fig. 7). Variance of η_{RW} is more than that of η_{LW} only in the frequency band of below 0.12 cpd, consistent with Davis and Bogden (1989). It becomes very low at high frequency because large-scale winds can be well-captured and high-frequency winds may be possibly canceled out in the employed basis functions.

Variance caused by remote winds ($\eta_{\Delta RL}$ in Fig. 8b) has a red spectrum, in particular, and contains dominant signals at low frequency band below 0.2 cpd. The residual SSHAs (η_{RWR} in Fig. 8b) are expected to contain the baroclinic tidal energy (e.g., nonlinear interactions at K_1 and M_2) and nonlinear mechanism between wind stress and SSHAs.

The wind skill of SSHAs using most NDBC winds off the USWC using multivariate regression varies 0.1 to 0.2 in southern and central California and 0.3 to 0.5 in northern

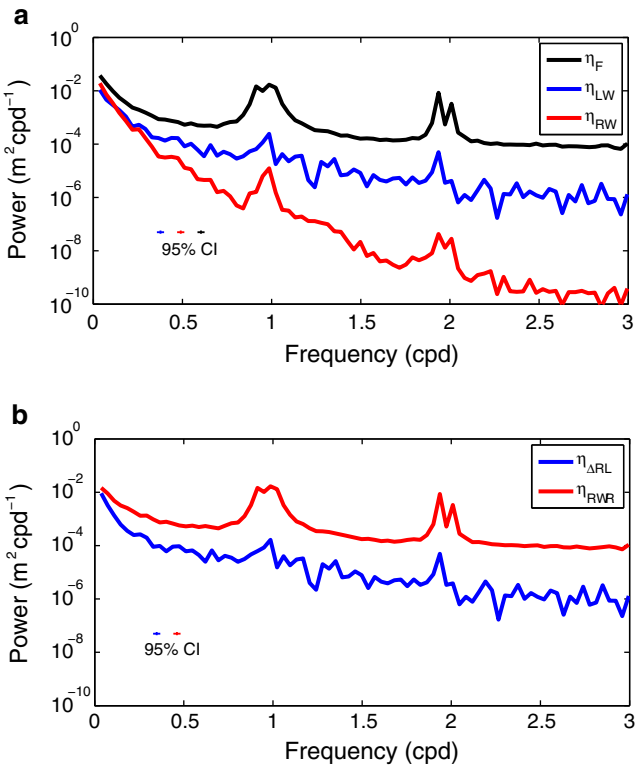

Fig. 8 Energy spectra of **a** SSHAs (η_F), local wind-coherent SSHAs (η_{LW}), and remote wind-coherent SSHAs (η_{RW}), **b** purely remote wind-coherent SSHAs ($\eta_{\Delta RL}$) and residual SSHAs (η_{RWR}) at Crescent City (T5 in Fig. 1). The 95 % confidence interval (CI) of individual spectra is indicated

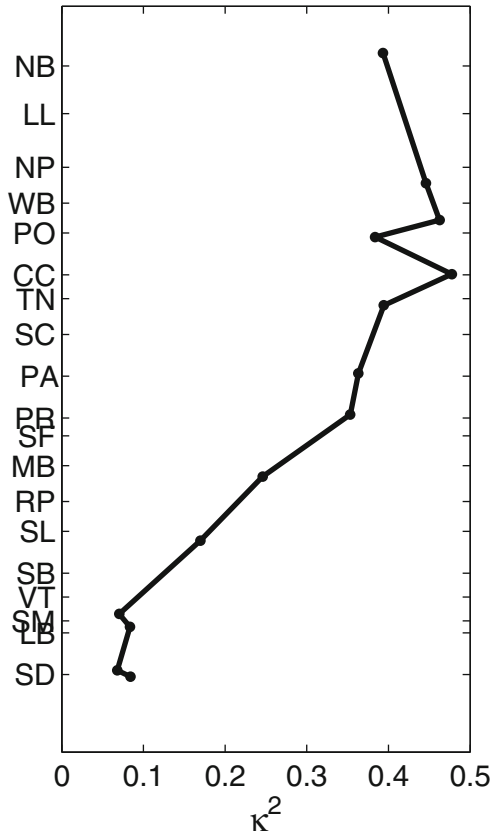

Fig. 9 Cross-validated wind skill when winds at 14 NDBC buoys off the USWC are used as basis functions the multivariate regression on the local SSHAs. The wind skill is only counted in the low frequency band ($\sigma \leq 0.4$ cpd)

California, Oregon, and Washington (Fig. 9), which is consistent with the wind skill of high-frequency radar-derived surface currents (e.g., Kim et al. 2011). The skill in other frequency bands (e.g., $\sigma \leq 1$ cpd or $\sigma \leq 3$ cpd) has a similar alongshore structure with the reduced skill compared to the skill at low frequency because of the low SNR at high frequency (not shown). The cross-validated skill at low frequency ($\sigma \leq 0.4$ cpd) will become an upper bound of this statistical analysis.

5 Discussion

5.1 Comparison of data-derived transfer functions

By Ryan and Noble (2006), G_y was fitted with a log linear function,

$$G_y(\sigma) = b + a \log_{10} \sigma, \tag{23}$$

where a and b are regression coefficients and they were reported as all negative values in the low frequency band ($0.0151 \leq \sigma \leq 0.3804$ cpd) (see Fig. 6 in Ryan and Noble (2006)). When Eq. 23 is plotted in the same way of Fig. 5, it has a convex shape as opposed to a red spectrum of concave shape. It is safe and appropriate to interpret G_y as a shape of the red spectrum due to limitations on resolving low frequency contents with finite observations.

5.2 Limitations on linear and frequency domain regression analysis

The regression in the frequency domain can be limited by a trade-off between the desired frequency resolution and confidence level of estimates. As the DOF increases, the frequency resolution of the estimates coarsens while the error bars become smaller (e.g., Kim et al. 2010a). This limits the interpretation of transfer functions at low frequency (e.g., climate indices). Ryan and Noble (2006) divided a single time series into subsegment time series with an equal length (e.g., ~60 days) in order to increase degrees of freedom and to maintain uncertainty in the estimates. This short individual time series may not differentiate variance at the multi-decadal cycles such as climate indices of ENSO, Pacific Decadal Oscillation (PDO), North Pacific Gyre Oscillation (NPGO). Moreover, at low frequency ($\sigma \leq 0.2$ cpd) Θ_y and Ω_y may not be constant as Ryan and Noble (2006) reported. While dynamics between wind stress and SSHAs can be assumed to be linear, especially, at low frequency (e.g., Davis and Bogden 1989), the phase may not have a linear relationship in that frequency band. On the other hand, a multivariate regression in the time domain (e.g., Chelton et al. 1988; Hill et al. 2007) can complement the analysis in this paper. As the wind transfer function is based on a linear system between wind stress and SSHAs, the nonlinear mechanism may not be included (e.g., Davis and Bogden 1989).

5.3 Extension to three-dimensional simulations

The idealized two-dimensional model adopted in the paper was used as a tool to examine the primary relationships in the wind-driven coastal circulation. A simple bathymetry, exclusion of alongshore dynamics, and idealized spatially uniform wind forcing were implemented in the model, which could provide a succinct view on the dynamical components and terms in the momentum equations. On the other hand, three-dimensional realistic numerical simulations and data-assimilated products may better describe the pressure gradients due to local and remote winds (e.g., Verdy et al.2013; Kim et al. 2013a). The spatial maps and vertical sections of components in momentum equations including pressure gradients can be available. However, the mixing parameterization in the surface layer and the influence of nonlinear terms may require a careful analysis and justification.

6 Conclusions

Local and remote wind-coherent responses of SSHs are examined with both statistical and analytical models. These two approaches complement to describe and characterize the system, primarily a linear system between driving forces and responses. The data-derived wind transfer functions are computed from surface wind stress at NDBC buoys and SSHAs at shoreline tide gauges for 15 years (1995 to 2009) off the USWC. On the other hand, the model-derived transfer functions are estimated from a two-dimensional analytical model constrained by the coastal boundary. Both data- and model-derived transfer functions are consistent at low frequency ($\sigma \leq 0.4$ cpd) and have some discrepancy at other frequencies due to incoherent signals and low SNR.

Based on a progressive and systematic regression using a single and multiple basis functions—a modified expectation maximization, the cross-validated skill increases and becomes saturated as the number of basis functions increases, demonstrating the influence of local and remote winds. The skill computed from all available winds off the USWC has a maximum as 0.1 in southern California, 0.2 to 0.3 in central California, and 0.3 to 0.5 in northern California, Oregon, and Washington. However, there is ambiguity in describing the contribution of each basis in the multivariate regression. While the physical distance between sampling locations of SSHs and wind stress can be the prior information (or weighting factor) of the estimate, it was not included in the analysis.

The wind-driven coastal circulation can be anisotropic and asymmetric due to pressure gradients driven by local and remote winds. The pressure setup can vary with the angle between the coastline and the wind direction, which modifies the phase of the wind transfer function. For instance, the terms in momentum equations and their spectral distribution in the frequency domain can be mirrored in x and y directions as the angle varies from 0° to 90°. As the transfer function is presented as a function of frequency and local depth, it can be used as a tool to examine the geostrophic and frictional balances of wind-driven circulation restricted by coastal boundaries. In other words, the influence of bottom friction becomes significant at the shallow depth ($h < \delta_E$; δ_E is the Ekman depth) and the transition frequency (σ_s), which indicates the dominance of geostrophic balance and frictional balance, was used.

The wind-driven SSHAs off the USWC have poleward propagating features and their phase speeds are in a range of 100 to 300 km day^{-1}, consistent with phase speeds of coastally trapped waves (e.g., Brink 1991; Kim et al. 2013b). Moreover, the residual SSHAs, incoherent components with all available coastal winds off the USWC, also contain the poleward propagating features in the similar order of magnitudes.

Acknowledgments Sung Yong Kim is supported by the Human Resources Development of the Korea Institute of Energy Technology Evaluation and Planning (KETEP), Ministry of Trade, Industry and Energy (no. 20114030200040) and the Basic Science Research Program through the National Research Foundation (NRF), Ministry of Education (no. 2013R1A1A2057849), Republic of Korea. The sea surface height data and harmonic constituents are provided by the Center for Operational Oceanographic Products and Services (CO-OPS) in NOAA. Wind at the NDBC buoy is available online at http://www.ndbc.noaa.gov/. The author thanks Bruce D. Cornuelle for discussion on the inverse problem with missing predictor and Timothy Ray for initial editorial comments.

Appendix A: Inverse problem with missing predictor

When an inverse problem given by the data ($\mathbf{d}$) and model predictor ($\mathbf{Z}$) is presented as

$$\mathbf{Zm} = \mathbf{d}, \tag{24}$$

the estimated model coefficients $(\hat{\mathbf{m}})$ are (e.g., Wunsch 1996)

$$\hat{\mathbf{m}} = \mathbf{PZ}^{\dagger}\left(\mathbf{ZPZ}^{\dagger} + \mathbf{R}\right)^{-1}\mathbf{d}, \tag{25}$$

$$= \left(\mathbf{Z}^{\dagger}\mathbf{R}^{-1}\mathbf{Z} + \mathbf{P}^{-1}\right)^{-1}\mathbf{Z}^{\dagger}\mathbf{R}^{-1}\mathbf{d}, \tag{26}$$

where $\mathbf{P}$ and $\mathbf{R}$ are the model and error covariance matrices. Equations 25 and 26 are identical by matrix inversion lemma. Equation 26 corresponds to Eq. 6 if $\mathbf{R}^{-1}$ is put inside of the parenthesis in Eq. 26. Thus, $\mathbf{R_a} = \mathbf{RP}^{-1}$, which implies the inverse of signal-to-noise ratio.

However, when the model predictor ($\mathbf{Z}$) is partially missing or containing unreliable values, the model coefficients ($\hat{\mathbf{m}}$) can be estimated with the modified error covariance ($\bar{\mathbf{R}}$) and the zero padded model predictor ($\bar{\mathbf{Z}}$) that compensates the incomplete predictor as below:

$$\hat{\mathbf{m}} = \left(\bar{\mathbf{Z}}^{\dagger}\bar{\mathbf{R}}^{-1}\bar{\mathbf{Z}} + \mathbf{P}^{-1}\right)^{-1}\bar{\mathbf{Z}}^{\dagger}\bar{\mathbf{R}}^{-1}\mathbf{d}, \tag{27}$$

where

$$\bar{\mathbf{Z}} = [\bar{z}_1\ \bar{z}_2\ \cdots\ \bar{z}_M], \tag{28}$$

$$\bar{\mathbf{R}} = \mathbf{R_b} + \sum_{k=1}^{M} h_k\, p_k, \tag{29}$$

$\bar{z}_k$ and p_k are the kth column vector of $\bar{\mathbf{Z}}$ and $\mathbf{P}$, respectively. h_k can be a constant value ($\langle\tilde{z}_k^2\rangle$) or Gaussian random variables with its mean ($\langle\tilde{z}_k^2\rangle$) and STD $\left(\sqrt{\langle\left(\tilde{z}_k^2\right)^2\rangle}\right)$. $\tilde{z}_k$ indicates the elements excluding missing or unreliable predictors in the kth column vector of $\bar{\mathbf{Z}}$. The magnitude of Fourier coefficients of wind stress are suggested as the prior ($\mathbf{P}$), and $\mathbf{R_b}$ is the noise level at each frequency. This approach can be called as a modified EM (e.g., Orchard and Woodbury 1972; Schneider 2001; Kim et al. 2011). The entries (or elements) of error covariance matrix ($\bar{\mathbf{R}}$)

corresponding missing predictors become penalized, using Eq. 29. A conservative way is to replace the entries in the covariance matrix with zeros.

Appendix B: Slow FFT

The evenly sampled data $[d(t_n)]$ are discrete Fourier transformed into $\hat{d}(\sigma_k)$ (regular FFT):

$$\hat{d}(\sigma_k) = \frac{1}{N} \sum_{n=0}^{N-1} d(t_n)\, e^{-i\sigma_k t_n} \tag{30}$$

and its inverse is

$$d(t_n) = \sum_{k=0}^{N-1} \hat{d}(\sigma_k)\, e^{i\sigma_k t_n}, \tag{31}$$

where $\sigma_k = 2\pi f_k$.

For the finite time series having discrete, continuous, and evenly sampled N records, the finite frequency axis is defined as

$$f_k = \Delta\sigma \left(k - N^* - 1\right), \tag{32}$$

where $N^* = \lfloor N/2 \rfloor$ $(k = 1, 2, \cdots, N)$. $\lfloor \cdot \rfloor$ denotes the greatest integer function (or floor function): $\lfloor x \rfloor = \max\{m \in \mathcal{Z} \mid m \le x\}$ and

$$\Delta\sigma = \frac{N-1}{N} \frac{1}{t_N - t_1}. \tag{33}$$

The slow FFT formulates the given time series (**d**) with trigonometric functions (**Z**) at entire finite frequencies (Eq. 31). The Fourier coefficients (**m**) can be computed by solving an inverse problem (Eqs. 25 and 26). For the biased estimate in the inverse problem, the prior (**P**) can be the Fourier coefficients of demeaned time series with zeros filled for the missing data, and the error (**R**) can be the SNR of the time series.

References

Agnew DC (1986) Detailed analysis of tide gauge data: a case history. Mar Geodesy 10:231–255

Allen JS (1980) Models of wind-driven currents on the continental shelf. Annu Rev Fluid Mech 12:389–433. doi:10.1146/annurev.fl.12.010180.002133

Allen JS, Denbo DW (1984) Statistical characteristics of the large-scale response of coastal sea level to atmospheric forcing. J Phys Oceanogr 14:1079–1094

Allen J, Newberger P, Federiuk J (1995) Upwelling circulation on the Oregon continental shelf. Part I: response to idealized forcing. J Phys Oceanogr 25:1843–1866

Atkins NT, Wakimoto RM (1997) Influence of the synoptic-scale flow on sea breezes observed during CaPE. Mon Wea Rev 125:2112–2130

Austin J, Lentz S (2002) The inner shelf response to wind-driven upwelling and downwelling. J Phys Oceanogr 32(7):2171–2193

Bendat J, Piersol AG (2000) Random data analysis and measurement procedures, 3rd edn. Wiley, New York

Brink KH (1991) Coastal-trapped waves and wind-driven currents over the continental shelf. Annu Rev Fluid Mech 23:389–412. doi:10.1146/annurev.fl.23.010191.002133

Brink KH (1998) The sea: the global coastal ocean: processes and methods. Wind-driven currents over the continental shelf, vol 10, chap. 1. Harvard University Press, Cumberland, RI 02864, pp 3–20

Brink KH, Allen JS, Smith R (1978) A study of low-frequency fluctuations near the Peru coast. J Phys Oceanogr 8(6):1025–1041

Brink KH, Stuart DW, van Leer JC (1984) Observations of the coastal upwelling region near 34°30′N off California: Spring 1981. J Phys Oceanogr 14(2):378–391

Caldwell PC, Stuart DW, Brink KH (1986) Mesoscale wind variability near point conception, California during Spring 1983. J Clim Appl Meteo 25:1241–1254

Cartwright D (1968) A unified analysis of tides and surges round north and east Britain. Philos Trans Roy Soc London Ser A Math Phys Sci 263(1134):1–55

Castelao RM, Barth JA (2005) Coastal ocean response to summer upwelling favorable winds in a region of alongshore bottom topography variations off Oregon. J Geophys Res 110:C10S04. doi:10.1029/2004JC002409

Chapman DC (1987) Application of wind-forced, long, coastal-trapped wave theory along the California coast. J Geophys Res 92(C2):1798–1816. doi:10.1029/JC092iC02p01798

Chelton DB, Enfield DB (1986) Ocean signals in tide gauge records. J Geophys Res 91(B9):9081–9098

Chelton DB, Bratkovich AW, Bernstein RL, Kosro PM (1988) Poleward flow off central California during the spring and summer of 1981 and 1984. J Geophys Res 93(C9):10,604–10,620

Chelton DB, Schlax MG, Samelson RM (2007) Summertime coupling between sea surface temperature and wind stress in the California current system. J Phys Oceanogr 37(3):495–517

Clarke AJ (1977) Observational and numerical evidence for wind-forced coastal trapped long waves. J Phys Oceanogr 7:231–247

Clarke AJ, Lebedev A (1999) Remotely driven decadal and longer changes in the coastal Pacific waters of the Americas. J Phys Oceanogr 29:828–835

Constable SC, Parker RL, Constable CG (1987) Ocean's inversion: a practical algorithm for generating smooth models from electromagnetic sounding data. Geophysics 52(3):289–300

Csanady G (1980) Longshore pressure gradients caused by offshore wind. J Geophys Res 85(C2):1076–1084. doi:10.1029/JC085iC02p01076

Davis RE (1985) Objective mapping by least squares fitting. J Geophys Res 90(C7):4773–4777. doi:10.1029/JC090iC03p04773

Davis RE, Bogden PS (1989) Variability on the California shelf forced by local and remote winds during the coastal ocean dynamics experiment. J Geophys Res 94(C4):4763–4783. doi:10.1029/JC094iC04p04763

Dever E (1997) Wind-forced cross-shelf circulation on the northern California shelf. J Phys Oceanogr 27(8):1566–1580

Dorman CE, Winant CD (1995) Buoy observations of the atmosphere along the West coast of the United States, 1981–1990. J Geophys Res 100(C8):16,029–16,044. doi:10.1029/95JC00964

Ebisuzaki W (1997) A method to estimate the statistical significance of a correlation when the data are serially correlated. J Clim 10(9):2147–2153

Efron B, Gong G (1983) A leisurely look at the bootstrap, the Jackknife, and the cross-validation. Am Stat 37(1):36–48

Ekman VW (1905) On the influence of the Earth's rotation on ocean-currents. Ark Mat Astron Fys 2:1–53
Emery WJ, Thomson RE (1997) Data analysis methods in physical oceanography. Elsevier
Enfield DB (1987) The intraseasonal oscillation in Eastern Pacific sea levels: how is it forced? J Phys Oceanogr 17(11):1860–1876
Enfield DB, Allen JS (1980) On the structure and dynamics of monthly mean sea level anomalies along the Pacific coast of North and South America. J Phys Oceanogr 10:557–578
Enfield DB, Allen JS (1983) The generation and propagation of sea level variability along the Pacific coast of Mexico. J Phys Oceanogr 13:1012–1033
Estoque MA (1961) A theoretical investigation of the sea breeze. Q J Roy Meteorol Soc 87:136–140. doi:10.1002/qj.49708737203
Flather R (1994) A storm surge prediction model for the northern Bay of Bengal with application to the cyclone disaster in April 1991. J Phys Oceanogr 24(1):172–190
Foreman R, Emeis S (2010) Revisiting the definition of the drag coefficient in the marine atmospheric boundary layer. J Phys Oceanogr 40:2325–2332. doi:10.1175/2010jpo4420.1
García-Reyes M, Largier JL (2010) Observations of increased wind-driven coastal upwelling off central California. J Geophys Res 115:C04011. doi:10.1029/2009JC005576
Garratt JR (1977) Review of drag coefficients over oceans and continents. Mon Wea Rev 105:915–929
Gay PS, Chereskin TK (2009) Mean structure and seasonal variability of the poleward undercurrent off southern California. J Geophys Res 114:C02007. doi:10.1029/2008JC004886
Gill AE, Niiler PP (1973) The theory of the seasonal variability in the ocean. Deep Sea Res 20:141–177
Gill A, Schumann E (1974) The generation of long shelf waves by the wind. J Phys Oceanogr 4(1):83–90
Gonella J (1972) A rotary-component method for analysis in meteorological and oceanographic vector time series. Deep Sea Res 19:833–846
Halliwell GR Jr, Allen JS (1984) Large-scale sea level response to atmospheric forcing along the West Coast of North America, Summer 1973. J Phys Oceanogr 14:864–886
Halliwell GR Jr, Allen JS (1987) The large-scale coastal wind field along the West Coast of North America, 1981–1982. J Geophys Res 92:1861–1884
Harms SH, Winant CD (1994) Synthetic subsurface pressure derived from bottom pressure and tide gauge observations. J Atmos Ocean Technol 11:1625–1637
Heaps N (1969) A two-dimensional numerical sea model. Philos Trans Roy Soc London Ser A Math Phys Sci 265(1160):93–137. doi:10.1098/rsta.1969.0041
Heaps N (1983) Storm surges, 1967–1982. Geophys J R Astr Soc 74(1):331–376
Hickey BM, Pola NE (1983) The seasonal alongshore pressure gradient on the West Coast of the United States. J Geophys Res 88(C12):7623–7633. doi:10.1029/JC088iC12p07623
Hill E, Ponte R, Davis J (2007) Dynamic and regression modeling of ocean variability in the tide-gauge record at seasonal and longer periods. J Geophys Res 112(C5):C05007. doi:10.1029/2006JC003745
Huthnance JM (1981) Waves and currents near the continental shelf edge. Prog Oceanogr 10:193–226
Inman JR (1975) Resistivity inversion with ridge regression. Geophysics 40(5):798–817
Janowitz GS, Pietrafesa LJ (1980) A model and observations of time-dependent upwelling over the mid-shelf and slope. J Phys Oceanogr 10:1574–1583
Kalnay E, Kanamitsu M, Klstler R, Collins W, Deaven D, Gandin L, Iredell M, Saha S, Whitle G, Woollen J, Zhu Y, Chellah M, Ebisuzaki W, Higgins W, Janowak J, Mo K, Ropelewski C, Wang J, Leetmaa A, Jenne RR, Joseph D (1996) The NCEP/NCAR 40-year reanalysis project. Bull Amer Meteor Soc 77(3):437–471
Kim SY, Terrill EJ, Cornuelle BD (2007) Objectively mapping HF radar-derived surface current data using measured and idealized data covariance matrices. J Geophys Res 112:C06021. doi:10.1029/2006JC003756
Kim SY, Cornuelle BD, Terrill EJ (2009) Anisotropic response of surface currents to the wind in a coastal region. J Phys Oceanogr 39(6):1512–1533. doi:10.1175/2009JPO4013.1
Kim SY, Cornuelle BD, Terrill EJ (2010a) Decomposing observations of high-frequency radar derived surface currents by their forcing mechanisms: decomposition techniques and spatial structures of decomposed surface currents. J Geophys Res 115:C12007. doi:10.1029/2010JC006222
Kim SY, Cornuelle BD, Terrill EJ (2010b) Decomposing observations of high-frequency radar derived surface currents by their forcing mechanisms: locally wind-driven surface currents. J Geophys Res 115:C12046. doi:10.1029/2010JC006223
Kim SY, Terrill EJ, Cornuelle BD, Jones B, Washburn L, Moline MA, Paduan JD, Garfield N, Largier JL, Crawford G, Kosro PM (2011) Mapping the U.S. West coast surface circulation: a multiyear analysis of high-frequency radar observations. J Geophys Res 116:C03011. doi:10.1029/2010JC006669
Kim SY, Gopalakrishnan G, Ponte A (2013a) Interpretation of anisotropic wind transfer functions using momentum balance derived from an idealized numerical model. Submitted
Kim SY, Cornuelle BD, Terrill EJ, Jones B, Washburn L, Moline MA, Paduan JD, Garfield N, Largier JL, Crawford G, Kosro PM (2013b) Poleward propagating subinertial alongshore surface currents off the U.S. West Coast. J Geophys Res 118. doi:10.1002/jgrc.20400
Kosro PM (1987) Structure of the coastal current field off Northern California during the coastal ocean dynamics experiment. J Geophys Res 92(C2):1637–1654. doi:10.1029/JC092iC02p01637
Lanczos C (1956) Applied analysis. Prentice-Hall, Eaglewood Cliffs
Large WG, Pond S (1981) Open ocean momentum flux measurements in moderate to strong winds. J Phys Oceanogr 11:324–336
Large WG, Morzel J, Crawford GB (1995) Accounting for surface wave distortion of the marine wind profile in low-level ocean storms wind measurements. J Phys Oceanogr 25:2959–2971
Largier JL, Magnell BA, Winant CD (1993) Subtidal circulation over the northern California shelf. J Geophys Res 98(C10):18,147–18,179. doi:10.1029/93JC01074
LeBlanc M, Tibshirani R (1996) Combining estimates in regression and classification. J Amer Stat Assoc 91(436):1641–1650
Lentz SJ (1993) The accuracy of tide-gauge measurements at subtidal frequencies. J Atmos Ocean Technol 10:238–245
Lentz SJ (1995) Sensitivity of the inner-shelf circulation to the form of the eddy viscosity profile. J Phys Oceanogr 25(1):19–28
Lentz SJ, Guza R, Elgar S, Feddersen F, Herbers T (1999) Momentum balances on the North Carolina inner shelf. J Geophys Res 104:18,205–18,226. doi:10.1029/1999JC900101
Lopez M, Clarke AJ (1989) The wind-driven shelf and slope water flow in terms of a local and a remote response. J Phys Oceanogr 19(8):1091–1101
Madsen OS (1977) A realistic model of the wind-induced Ekman boundary layer. J Phys Oceanogr 7:248–255
Mastenbroek C, Burgers G, Janssen P (1993) The dynamical coupling of a wave model and a storm surge model through the atmospheric boundary layer. J Phys Oceanogr 23(8):1856–1866
McCreary JP (1981) A linear stratified ocean model of the coastal undercurrent. Philos Trans Roy Soc London Ser A Math Phys Sci 302(1469):385–413

Mooers CNK, Smith RL (1968) Continental shelf waves off oregon. J Geophys Res 73(2):549–557. doi:10.1029/JB073i002p00549
Nicolle A, Karpytchev M, Benoit M (2009) Amplification of the storm surges in shallow waters of the Pertuis Charentais (Bay of Biscay, France). Ocean Dyn 59(6):921–935
O'Brien JJ, Clancy RM, Clarke AJ, Crepon M, Elsberry R, Gammelstød T, MacVean M, Rŏed LP, Thompson JD (1977) Modelling and prediction of the upper layers of the ocean, chap. Upwelling in the ocean: two- and three-dimensional models of upper ocean dynamics and variability, pp 178–228. Pergamon
Oppenheim AV, Schafter RW, Buck JR (1998) Discrete-time signal processing, 2nd edn. Prentice-Hall, Upper Saddle River
Orchard T, Woodbury MA (1972) A missing information principle: theory and applications. In: 6th Berkeley symposium on mathematics, statistics, and probability. California
Pares-Sierra A, O'Brien JJ (1989) The seasonal and interannual variability of the California current system: a numerical model. J Geophys Res 94(C3):3159–3180. doi:10.1029/JC094iC03p03159
Pawlowicz R, Beardsley B, Lentz S (2002) Classic tidal harmonic analysis including error estimates in MATLAB using T_TIDE. Comput Geosci 28:929–937
Platzman G (1979) A Kelvin wave in the eastern north Pacific ocean. J Geophys Res 84(C5):2525–2528. doi:10.1029/JC084iC05p02525
Pond S, Pickard G (1983) Introductory dynamical oceanography, 2nd edn. Butterworth-Heinemann
Ponte ALS (2009) Wind and tidal response of a semi-enclosed bay, Bahia Concepcion, Baja California. Ph.D. thesis, Scripps Institution of Oceanography
Ponte ALS (2010) Periodic wind-driven circulation in an elongated and rotating basin. J Phys Oceanogr 40:2043–2058. doi:10.1175/2010JPO4235.1
Priestley MB (1981) Spectral analysis and time series. Academic, London
Pringle JM (2002) Enhancement of wind-driven upwelling and downwelling by alongshore bathymetric variability. J Phys Oceanogr 32:3101–3112
Pringle J, Dever E (2009) Dynamics of wind-driven upwelling and relaxation between Monterey bay and point arena: Local-, regional-, and gyre-scale controls. J Geophys Res 114:C07003. doi:10.1029/2008JC005016
Ramp SR, Rosenfeld LK, Tisch TD, Hicks MR (1997) Moored observations of the current and temperature structure over the continental shelf off central California 1. A basic description of the variability. J Geophys Res 102(C10):22,877–22,902. doi:10.1029/97JC02329
Ryan HF, Noble M (2002) Sea level response to ENSO along the central California coast: how the 1997–1998 event compares with the historic record. Prog Oceanogr 54:149–169
Ryan HF, Noble MA (2006) Alongshore wind forcing of coastal sea level as a function of frequency. J Phys Oceanogr 36:2173–2184
Schneider T (2001) Analysis of incomplete climate data: estimation of mean values and covariance matrices and imputation of missing values. J Clim 14:853–871
Singer IA (1967) Steadiness of the wind. J Appl Meteorol 6:1033–1038
Skyllingstad ED, Barbour P, Dorman CE (2001) The dynamics of northwest summer winds over the Santa Barbara Channel. Mon Wea Rev 129(5):1042–1061
Spillane MC, Enfield DB, Allen JS (1987) Intraseasonal oscillations in sea level along the West coast of the Americas. J Phys Oceanogr 17(3):313–325
Strub PT, James C (1988) Atmospheric conditions during the spring and fall transitions in the coastal ocean off Western United States. J Geophys Res 93(C12):15,561–15,584. doi:10.1029/JC093iC12p15561
Strub PT, Allen JS, Huyer A, Smith RL, Beardsley RC (1987) Seasonal cycles of currents, temperatures, winds, and sea level over the northeast Pacific continental shelf: 35°N to 48°N. J Geophys Res 92(C2):1507–1526. doi:10.1029/JC092iC02p01507
Tikhonov AN, Arsenin VY (1977) Solutions of ill-posed problems. Wiley, New York
van den Dool HM, Saha S, Johansson Å (2000) Empirical orthogonal teleconnections. J Clim 13:1421–1435
Verdy A, Mazloff M, Cornuelle BD, Kim SY (2013) Wind-driven sea level variability on the california coast: an adjoint sensitivity analysis. J Phys Oceanogr. doi:10.1175/JPO-D-13-018.1
von Storch H, Zwiers F (1999) Statistical analysis in climate research. Cambridge University Press, Cambridge
Wang DP, Mooers CNK (1977) Long coastal-trapped waves off the West Coast of the United States, Summer 1973. J Phys Oceanogr 7:856–864
Weisberg RH, Li Z, Muller-Karger R (2001) West Florida shelf response to local wind forcing: April 1998. J Geophys Res 106(C12):31,239–31,262. doi:10.1029/2000JC000529
Weller RA (1981) Observations of the velocity response to wind forcing in the upper ocean. J Geophys Res 86(C3):1969–1977
Winant CD (1980) Coastal circulation and wind-induced currents. Annu Rev Fluid Mech 12:271–301. doi:10.1146/annurev.fl.12.010180.001415
Winant CD (2004) Three-dimensional wind-driven flow in an elongated rotating basin. J Phys Oceanogr 34:462–476
Winant C (2006) Three-dimensional wind-driven coastal circulation past a headland. J Phys Oceanogr 36(7):1430–1438
Winant C (2007) Three-dimensional tidal flow in an elongated, rotating basin. J Phys Oceanogr 37(9):2345–2362
Winant CD, Dorman CE (1997) Seasonal patterns of surface wind stress and heat flux over the Southern California bight. J Geophys Res 102(C3):5641–5653. doi:10.1029/96JC02801
Winant CD, Dever EP, Hendershott MC (2003) Characteristic patterns of shelf circulation at the boundary between central and southern California. J Geophys Res 108(C2):3021. doi:10.1029/2001JC001302
Wooster WS, Jones JH (1970) California undercurrent of Northern Baja California. J Mar Res 28:235–250
Wunsch C (1996) The ocean circulation inverse problem. Cambridge University Press, New York
Wunsch C, Stammer D (1997) Atmospheric loading and the oceanic inverted barometer effect. Rev Geophys 35:79–107. doi:10.1029/96RG03037
Yelland M, Taylor PK (1996) Wind stress measurements from the open ocean. J Phys Oceanogr 26:541–558